Interlayer-Engineered Schottky Barrier and Rectification at Metal/β-Ga_2O_3 Interfaces from First Principles*

Tianyu Lin(林天誉)[1,2,3], Wenjie Yin(殷文杰)[1,2,3], Zhiqiang Fan(范志强)[4†]
Yuxiong Long(龙宇雄)[1,2,3‡] and Jiayu Dai(戴佳钰)[1,2,3§]
[1]College of Science, National University of Defense Technology,
Changsha 410073, China
[2]Hunan Key Laboratory of Extreme Matter and Applications,
National University of Defense Technology, Changsha 410073, China
[3]Hunan Research Center of the Basic Discipline for Physical States,
National University of Defense Technology, Changsha 410073, China
[4]School of Physics and Electronic Science,
Changsha University of Science and Technology, Changsha 410114, China

October 16, 2026

Abstract

Using DFT-NEGF simulations with the TB-mBJ exchange potential, we investigate Schottky barrier formation and carrier transport in metal/β-Ga_2O_3(100) contacts. For Ni, Ti, Ag, and Au contacts at a donor concentration of $1 \times 10^{19}\,\mathrm{cm}^{-3}$, Au exhibits pronounced forward rectification, while Ag, Ti, and Ni display degraded or reversed rectification due to metal-induced gap states (MIGS) that enhance Fermi-level pinning and tunneling. Inserting a monolayer hexagonal boron nitride (h-BN) interlayer into the Ag contact suppresses MIGS, shifting the dominant transport mechanism from quantum tunneling to thermionic emission and restoring forward rectification. In contrast, a polar Janus WSSe interlayer creates an interfacial built-in electric field that yields reverse rectification relative to the h-BN-interlayered contact. However, the Janus-interlayered contact exhibits a small current. Reversing the WSSe orientation to WSeS changes the transport response, but the effect is not a simple mirror image. These results provide design rules for choosing metals, doping levels, and 2D interlayers to suppress MIGS and tailor Schottky rectification in ultra-wide-bandgap β-Ga_2O_3 electronics.

Keywords: ab initio quantum transport, Schottky Barrier Diode, contact engineering

PACS: 73.30.+y, 73.40.-c, 72.10.-d and 73.63.-b

*Project supported by the National Key Research and Development Program of China (Grant No. 2024YFA1408200), the National Natural Science Foundation of China (Grant Nos. 12404099, 2534013, and 12504326), and the Science and Technology Innovation Program of Hunan Province (Grant Nos. 2025ZYJ001 and 2021RC4026).

†Corresponding author. E-mail: zqfan@csust.edu.cn
‡Corresponding author. E-mail: yxlong@nudt.edu.cn
§Corresponding author. E-mail: jydai@nudt.edu.cn

1. Introduction

Ultra-wide-bandgap (UWBG) semiconductors are increasingly important for next-generation power and high-frequency electronic devices because of their high critical electric fields, low intrinsic carrier concentrations, and potential for operation under high-voltage and high-temperature conditions [1–4]. Among them, monoclinic β-Ga_2O_3 has emerged as a particularly promising UWBG semiconductor. It possesses a band gap of approximately 4.8–5.3 eV, a high theoretical breakdown field, and the important practical advantage that large-area bulk single crystals can be grown by melt-based methods [5–9]. These characteristics make β-Ga_2O_3 attractive for Schottky barrier diodes, field-effect transistors, and solar-blind photodetectors [10–14]. However, the performance of β-Ga_2O_3 power devices is often limited not only by the bulk material properties but also by carrier injection and transport at metal/semiconductor interfaces.

Metal/β-Ga_2O_3 Schottky contacts play a central role in determining the turn-on voltage, reverse leakage current, contact resistance, breakdown behavior, and rectification capability of electronic devices [11,15–18]. In an ideal Schottky–Mott picture, the barrier height is governed by the difference between the metal work function and the semiconductor electron affinity. In practice, however, the barrier formation at metal/β-Ga_2O_3 interfaces is substantially more complicated. Interfacial atomic bonding, charge transfer, interface dipoles, surface termination, structural defects, and metal-induced gap states (MIGS) [19–22] can collectively alter the local electronic structure and cause Fermi-level pinning [23–26]. Consequently, changing the contact metal alone may not provide a predictable or sufficiently broad modulation of the Schottky barrier [27]. A microscopic understanding of the relationship among metal selection, interfacial states, barrier formation, and nonequilibrium carrier transport is therefore essential for the rational design of high-performance β-Ga_2O_3 contacts [28].

Interface-layer engineering provides an effective route to overcome the limitations imposed by direct metal /semiconductor contact. Two-dimensional materials are especially attractive as ultrathin interlayers because they can modify interfacial coupling, suppress undesirable gap states, and introduce controllable dipoles without substantially increasing the device thickness [29]. Hexagonal boron nitride (h-BN), a wide-bandgap insulating two-dimensional material, can electronically decouple the metal from the semiconductor [30,31] and thereby reduce the penetration of MIGS into the semiconductor band gap. Such decoupling may alleviate Fermi-level pinning and recover a more favorable Schottky barrier for rectifying transport. In contrast, Janus transition-metal dichalcogenides possess an intrinsic out-of-plane polarity arising from the structural asymmetry of their two chalcogen layers [32–34]. Their built-in dipole can modify the interfacial electrostatic potential and barrier asymmetry, offering an additional degree of freedom for controlling carrier injection and rectification direction. Nevertheless, the distinct roles of an insulating h-BN interlayer and a polar Janus interlayer in metal/β-Ga_2O_3 contacts remain insufficiently understood, particularly from the perspective of bias-dependent quantum transport.

Interfaces are also central to the reliability of electronic devices, since interface states and dipoles govern band alignment, gate tunneling and dielectric reliability. Atomic-level studies of $Si/SiO_2/HfO_2$ stacks have shown that interface and surface dipoles control the band offsets and hence the tunneling current and device-to-device variation [35,36]; unified interface-dipole theories provide a general framework for the barrier-height trends at metal–semiconductor contacts [37]; and device-scale analyses of strain- and dipole-induced interface states [38], together with studies of Ga_2O_3 interface states [39] and of interface reliability [40], demonstrate how interface

states control transport and reliability in practical devices. For β-Ga_2O_3-based systems in particular, recent studies have shown that the band alignment can be engineered by surface selection [41] and that Fermi-level depinning and ideal metal contacts can be achieved by integrating two-dimensional metallic layers [42]. These works reinforce the motivation of the present study, in which interface dipoles (Janus interlayer) and interface states (MIGS) are used to tailor the Schottky barrier and the dominant transport mechanism.

In this work, we systematically investigate Schottky-barrier formation and carrier transport in Ni, Ti, Ag, and Au contacts on β-Ga_2O_3(100) using density functional theory combined with the nonequilibrium Green's function method. The TB-mBJ exchange potential is employed to obtain a reliable electronic structure for β-Ga_2O_3, and the effects of n-type doping on the transport behavior of the metal/β-Ga_2O_3 contacts are examined. We further explore two interface-engineering strategies based on h-BN and Janus WSSe interlayers, which act as an insulating spacer and a polar modifier, respectively. By comparing these configurations under identical doping conditions, we aim to clarify the interplay among metal selection, doping, MIGS, and interlayer-induced electrostatic modulation, and to provide theoretical guidance for interface design in β-Ga_2O_3-based UWBG electronic devices.

2. Computational Methods

2.1. First-Principles Calculations

All first-principles calculations were performed within the framework of density functional theory (DFT) [43]. Exchange-correlation effects were treated using the Perdew-Burke-Ernzerhof (PBE) generalized gradient approximation, with Fritz-Haber Institute (FHI) pseudopotentials and a double-zeta polarized (DZP) basis set. Structural optimization proceeded until the maximum residual force on each atom was below 0.02 eV Å^{-1}, with a total-energy convergence threshold of 10^{-5} eV. To overcome the well-known band gap underestimation of semilocal DFT for β-Ga_2O_3, the Tran-Blaha modified Becke-Johnson (TB-mBJ) exchange potential [44–46] was employed. The TB-mBJ parameter c was calibrated against the experimental band gap, and c = 1.14 reproduced the experimental indirect band gap of 4.85 eV, as can be seen in Figs. S1 and S2 of the supplementary material. This parameter was subsequently adopted for all electronic-structure and quantum transport calculations.

Metal/β-Ga_2O_3(100) interface models were constructed for Au, Ag, Ti, and Ni contacts as well as h-BN and Janus WSSe/WSeS interlayer configurations. For consistency, the in-plane lattice constants were fixed to those of β-Ga_2O_3, with the residual lattice mismatch accommodated by the metal layer. The resulting mismatches were 2.45%, 1.55%, 3.76%, and 1.58% for Ag, Ti, Ni, and Au, respectively, as listed in Table S2 of the supplementary material. All interfaces were constructed on the β-Ga_2O_3(100) B surface. Two terminations are possible for this surface, usually denoted A and B; the B termination is thermodynamically more stable than the A termination [47] and is therefore the surface expected to be realized under typical growth and processing conditions. The same (100) B surface is used in all devices, so that the comparison among different metals and interlayer configurations is performed under identical semiconductor conditions. The interfacial registry of all models is shown in Fig. 1, and the corresponding lattice parameters are summarized in Table S2 of the supplementary material.

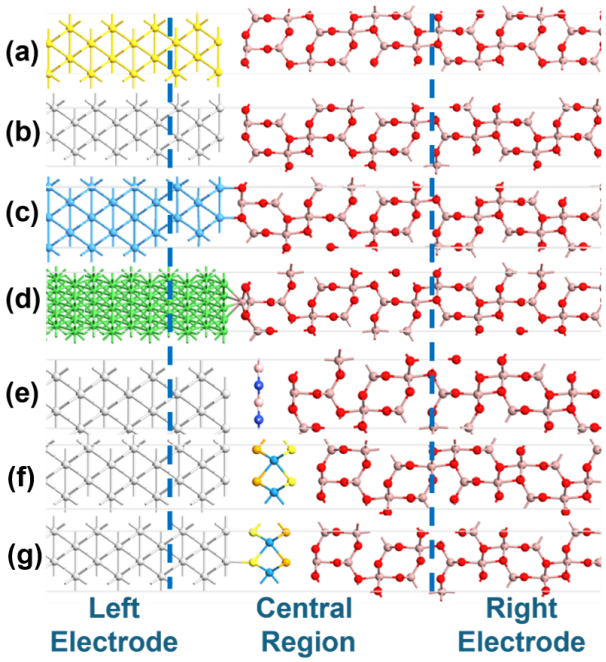


Figure 1: Interface model of metal/β-Ga_2O_3(100) contacts with and without 2D interlayers: (a) Au/β-Ga_2O_3, (b) Ag/β-Ga_2O_3, (c) Ti/β-Ga_2O_3, (d) Ni/β-Ga_2O_3, (e) Ag/h-BN/β-Ga_2O_3, (f) Ag/WSeS/β-Ga_2O_3, and (g) Ag/WSSe/β-Ga_2O_3.

2.2. Quantum Transport Calculations

Quantum transport properties were calculated within the density functional theory (DFT) combined with the nonequilibrium Green's-function (NEGF) formalism [48–50], as implemented in the QuantumATK [51] software package. The two-probe device consisted of semi-infinite metal and β-Ga_2O_3 electrodes with a fully relaxed scattering region in between. The transverse periodicity of the device cell perpendicular to the transport direction is $W = 0.284458$ nm, and all currents are reported per unit width in μA/μm. The length of the β-Ga_2O_3 region in the scattering region was set to 12 nm (120 Å), which is sufficient for the depletion region to develop fully within the simulated cell at all doping levels considered. The transverse Brillouin zone was sampled using a Γ-centered $6 \times 3 \times 1$ k-point mesh with an energy cutoff of 80 Hartree. Unless otherwise specified, transport calculations were performed at 300 K. n-type doping in β-Ga_2O_3 was introduced using the atomic compensation charge method with donor concentrations ranging from 1×10^{18} to $1 \times 10^{20}\,\mathrm{cm}^{-3}$. The current under an applied bias voltage was evaluated using the Landauer–Büttiker formalism,

$$I(V) = \frac{2e}{h} \int_{-\infty}^{+\infty} T(E,V)\,[f_{\mathrm{L}}(E,\mu_{\mathrm{L}},T) - f_{\mathrm{R}}(E,\mu_{\mathrm{R}},T)]\,dE, \tag{1}$$

where $T(E,V)$ is the transmission coefficient under bias, $f_{\mathrm{L(R)}}$ denotes the Fermi–Dirac distribution of the left (right) electrode, and $\mu_{\mathrm{L}} - \mu_{\mathrm{R}} = eV$. The transmission coefficient is given by

$$T(E,V) = \mathrm{Tr}\left[\Gamma_{\mathrm{L}} G^{r} \Gamma_{\mathrm{R}} G^{a}\right], \tag{2}$$

where $G^{r(a)}$ is the retarded (advanced) Green's function and $\Gamma_{\mathrm{L(R)}}$ is the electrode broadening matrix.

Finally, we specify the bias convention adopted throughout this work. The applied bias is defined via $\mu_{\mathrm{L}} - \mu_{\mathrm{R}}$. Under this convention, forward bias corresponds to $V = -0.3$ V, whereas reverse bias corresponds to $V = +0.3$ V. The rectification ratio is defined as $\mathrm{RR} = |I(-0.3\,\mathrm{V})|/|I(+0.3\,\mathrm{V})|$, where $I(-0.3\,\mathrm{V})$ and $I(+0.3\,\mathrm{V})$ are the currents under forward and reverse bias; $\mathrm{RR} > 1$ and $\mathrm{RR} < 1$ thus denote forward and reverse rectification, respectively. Schottky barrier heights (SBHs) were extracted from the projected local density of states (PLDOS) using the band-edge onset: the conduction-band edge E_C of the semiconductor was determined from the onset of the PLDOS in the β-Ga_2O_3 region adjacent to the interface, the Fermi level was taken from the electrode calculation.

3. Results and Discussion

3.1. Doping-Dependent Carrier Transport in Au/β-Ga_2O_3 Contacts

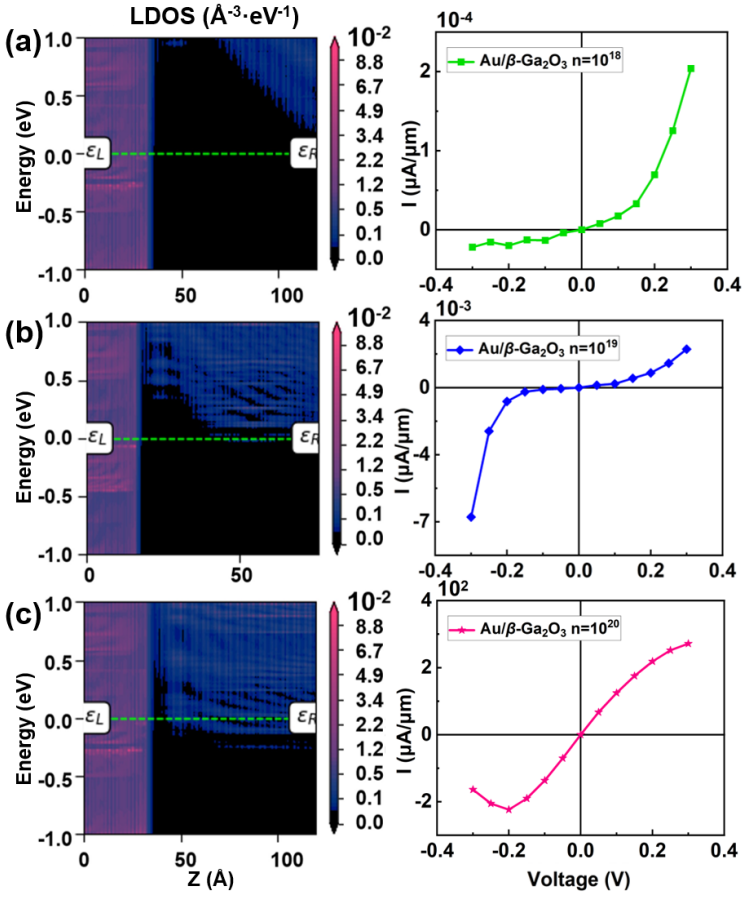


Figure 2: PLDOS and I–V transport characteristics of Au/β-Ga_2O_3 devices with donor concentrations of (a) $1 \times 10^{18}\,\mathrm{cm}^{-3}$, (b) $1 \times 10^{19}\,\mathrm{cm}^{-3}$, and (c) $1 \times 10^{20}\,\mathrm{cm}^{-3}$.

We first consider the Au/β-Ga_2O_3 contact as a reference system because its relatively weak MIGS preserve a well-defined Schottky barrier, allowing the intrinsic effect of donor concentration on carrier transport to be isolated. Fig. 2 shows the I–V characteristics of the Au/β-Ga_2O_3 contact calculated for the two-probe setup at low ($n_d = 10^{18}\,\mathrm{cm}^{-3}$), intermediate ($n_d = 10^{19}\,\mathrm{cm}^{-3}$) and high ($n_d = 10^{20}\,\mathrm{cm}^{-3}$) donor concentrations. As

shown in Fig. 2(a–c), increasing the donor concentration systematically drives the transport characteristics from reverse rectification at $1 \times 10^{18}\,\mathrm{cm}^{-3}$, to conventional Schottky rectification at $1 \times 10^{19}\,\mathrm{cm}^{-3}$, and finally to quasi-ohmic behavior at $1 \times 10^{20}\,\mathrm{cm}^{-3}$, as summarized in Table S3 of the supplementary material.

The underlying mechanism is revealed by the spectral current, projected local density of states (PLDOS), and effective potential profiles. At the intermediate donor concentration of $1 \times 10^{19}\,\mathrm{cm}^{-3}$, carrier transport is dominated by thermionic-emission-like injection under forward bias and by quantum tunneling under reverse bias, resulting in pronounced forward rectification with a rectification ratio of ∼3.37 at ±0.3 V (the current reaches $\sim 6.7\times10^{-3}$ μA/μm at −0.3 V versus $\sim 2.0\times10^{-3}$ μA/μm at +0.3 V). Reducing the donor concentration widens the depletion region and suppresses thermionic transport. Meanwhile, the narrower effective barrier under reverse bias enhances tunneling, corresponding to a rectification ratio of only ∼0.13 and thereby reversing the rectification polarity. In contrast, increasing the donor concentration significantly narrows the depletion region, promoting tunneling under both bias polarities and consequently reducing the current asymmetry to a rectification ratio of only ∼0.60, leading to quasi-ohmic transport.

These results establish donor concentration as an effective parameter for controlling the competition between thermionic emission and quantum tunneling through modulation of the depletion region and effective Schottky barrier. Among the investigated doping levels, $1 \times 10^{19}\,\mathrm{cm}^{-3}$ provides the optimum balance between efficient forward carrier injection and suppressed reverse-bias tunneling, resulting in the strongest rectifying behavior. Convergence tests with respect to the device length confirm that the effective potential profile is fully converged for all doping levels, including the lowest donor concentration of $1 \times 10^{18}\,\mathrm{cm}^{-3}$.

3.2. Metal-Dependent Schottky Barrier Formation and Carrier Transport

To reveal the microscopic origin of the metal-dependent transport behavior, Au, Ag, Ti, and Ni contacts on n-type β-Ga_2O_3(100) were compared at a fixed donor concentration of $1\times10^{19}\,\mathrm{cm}^{-3}$. Although all contacts share the same semiconductor orientation and doping condition, their rectification characteristics differ substantially: as shown in Fig. 2(b) and Fig. 3(a–c), Au exhibits pronounced forward rectification with a rectification ratio of ∼3.37 at ±0.3 V, whereas Ag and Ti show degraded or reversed rectification with rectification ratios of ∼0.22 and ∼0.69, respectively, and Ni displays weak rectification with a rectification ratio of ∼0.37. The calculated Schottky barrier heights are 0.340 eV, 0.145 eV, 0.321 eV, and 2.1 eV for Au, Ag, Ti, and Ni, respectively, as can be seen in Table S3 of the supplementary material. These values characterize the idealized interface structures and doping conditions employed here and are intended as a qualitative reference rather than a quantitative prediction; we therefore focus on the relative trends and the underlying physical mechanisms. These results demonstrate that the electrical behavior of β-Ga_2O_3 Schottky contacts cannot be solely explained by the metal work function. Instead, the transport response is governed by the metal-dependent interfacial electronic structure, which determines the extent of Fermi-level pinning, the effective barrier profile, and the contribution of interface-assisted tunneling pathways.

The metal-dependent transport behavior is closely associated with the strength and spatial extension of MIGS at the interface. As revealed by the PLDOS in Fig. 3, metal–β-Ga_2O_3 hybridization generates gap states whose penetration depth varies significantly among different metals. Extended MIGS increase the interfacial density of states near the Fermi level, resulting in stronger Fermi-level pinning and weakening the sensitivity of

the effective Schottky barrier to the metal work function. More importantly, MIGS extending into the semiconductor depletion region reshape the local tunneling barrier and introduce additional transmission channels, which enhances leakage current and suppresses rectification.

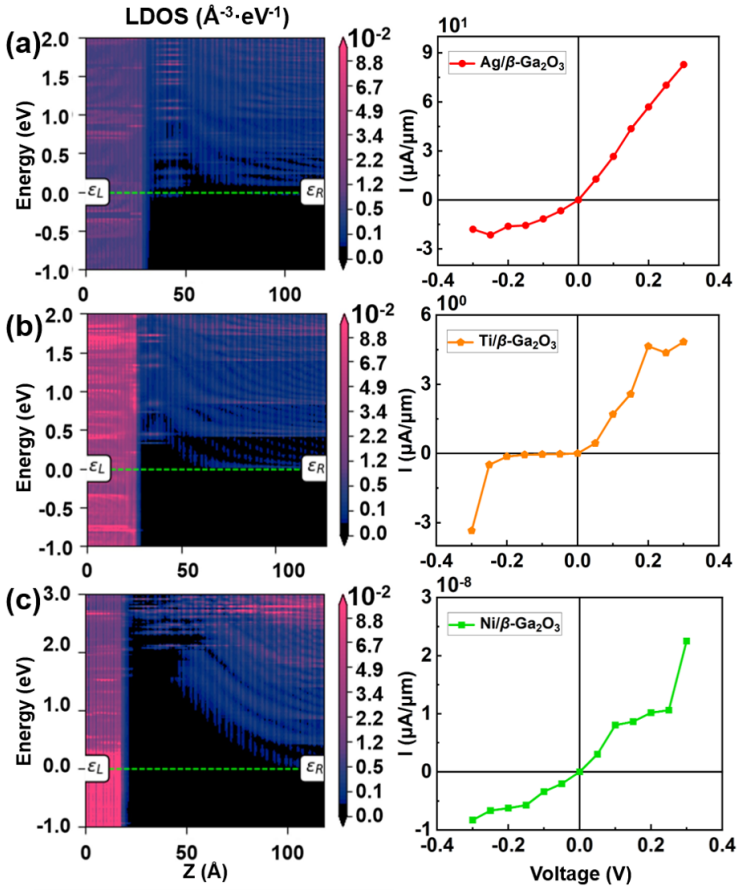


Figure 3: PLDOS and I–V transport characteristics for different metal/β-Ga_2O_3 interfaces: (a) Ag/β-Ga_2O_3, (b) Ti/β-Ga_2O_3, and (c) Ni/β-Ga_2O_3.

Among the investigated contacts, Au/β-Ga_2O_3 retains the most favorable balance between barrier formation and carrier injection. Its comparatively weak interfacial-state contribution preserves a discernible Schottky barrier and limits MIGS-assisted leakage. Consequently, the current under forward bias is enhanced relative to that under reverse bias, producing the conventional rectifying behavior in Fig. 2(b). In conjunction with the doping-dependent results discussed above, this behavior identifies Au as the most suitable metal among those considered for achieving forward rectification at $1 \times 10^{19}\,\mathrm{cm}^{-3}$.

In contrast, the Ag/β-Ga_2O_3 contact exhibits pronounced MIGS penetration and strong Fermi-level pinning. Fig. 4 shows the layer-resolved PDOS revealing the penetration depth of Ag- and Au-derived MIGS extending into the β-Ga_2O_3 band gap. As shown in Fig. 4, Ag-derived states extend deeply into the semiconductor band gap, increasing the interfacial density of states and weakening the effective Schottky barrier; consequently, the contact exhibits degraded and eventually reversed rectification, as seen in Fig. 3(a). To quantify the spatial penetration of the MIGS, we integrated the layer-resolved PDOS of each β-Ga_2O_3 layer over a small energy window around the Fermi level, $Q_{\mathrm{gap}}(d) = \int_{E_F-W}^{E_F+W} \rho_d(E)\,\mathrm{d}E$ (with $W = 0.05$ eV), and fitted the resulting profile to an exponential decay, $Q_{\mathrm{gap}}(d) = Q_0 \exp(-d/\lambda)$. The resulting layer-resolved

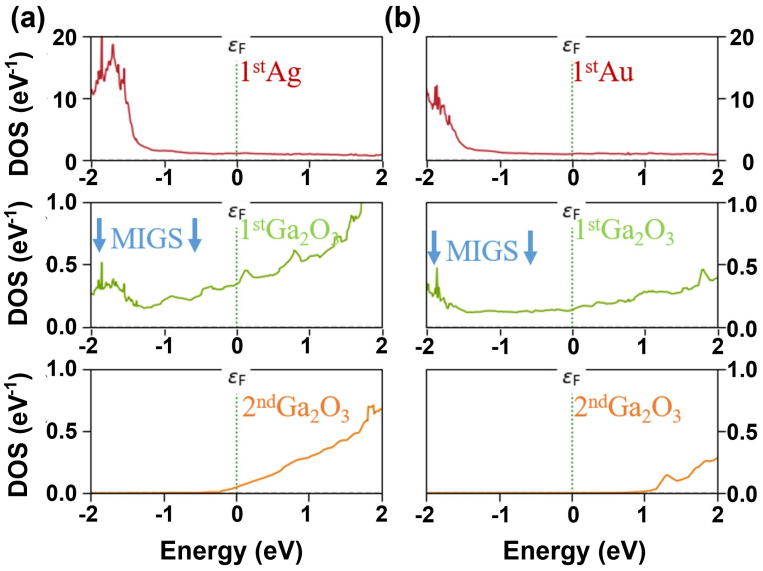


Figure 4: Layer-resolved PDOS of metal and β-Ga_2O_3 individual layers for (a) Ag/β-Ga_2O_3 and (b) Au/β-Ga_2O_3.

spectral weights and the corresponding exponential fits are shown in Fig. S5 of the supplementary material; the extracted decay lengths are $\lambda \approx 9.7$ Å for Ag, 1.5 Å for Au and 1.93 Å for Ag/h-BN (changing by at most 1.9, 0.02 and 0.1 Å, respectively, when the energy window used for the integration is varied), with interfacial amplitudes Q_0 of 3.4×10^{-4}, 1.2×10^{-2} and 2.87×10^{-4} eV^{-1}. More importantly, the in-gap density of states at the Fermi level differs by more than an order of magnitude: $D_{\mathrm{gap}}(E_F) \approx 1.8 \times 10^{-3}$ for Ag, 4.7×10^{-4} for Au and 1.1×10^{-4} for Ag/h-BN (in units of eV^{-1}). The long decay length and the large $D_{\mathrm{gap}}(E_F)$ of the bare Ag contact show that its MIGS penetrate deeply into the semiconductor and supply a high density of interface states near E_F, which pins the Fermi level and weakens the effective barrier (0.145 eV); the Au contact, whose gap states decay over only ∼1.5 Å and give a smaller $D_{\mathrm{gap}}(E_F)$, preserves a well-defined barrier (0.340 eV) and forward rectification. Inserting the h-BN monolayer reduces $D_{\mathrm{gap}}(E_F)$ by more than an order of magnitude and restores both the barrier (0.179 eV) and forward rectification, quantitatively confirming the suppression of MIGS inferred from the PLDOS. The Ti and Ni contacts further demonstrate the sensitivity of transport to the interfacial electronic structure. For Ti/β-Ga_2O_3, the interface states and resulting barrier profile promote substantial non-thermionic carrier transmission, leading to poor or reverse rectification revealed in Fig. 3(b). In contrast, Ni/β-Ga_2O_3 exhibits a nearly symmetric current response, indicating that the interfacial states substantially reduce the difference between forward and reverse transport pathways as shown in Fig. 3(c).

Overall, the metal-dependent transport behavior follows a clear interface-to-transport relationship. The metal orbital character governs the strength and spatial decay of MIGS, which in turn determines Fermi-level pinning, effective barrier modulation, and tunneling transmission. Consequently, Au preserves a barrier profile favorable for forward rectification, whereas Ag, Ti, and Ni exhibit degraded rectification due to enhanced interface-state-mediated transport.

3.3. Interlayer Engineering: MIGS Suppression and Polarization-Controlled Transport

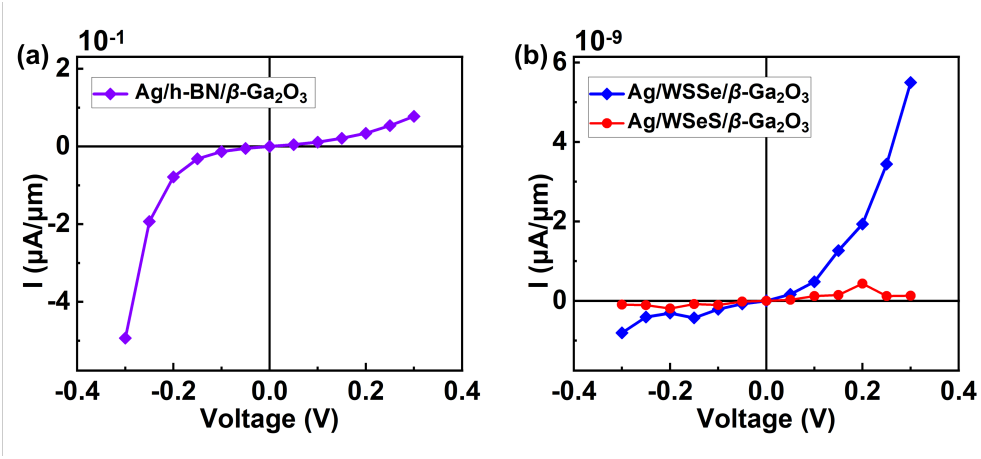


Figure 5: I–V transport characteristics of Ag-based contacts with different interlayers: (a) Ag/h-BN/β-Ga_2O_3, (b) Ag/WSSe/β-Ga_2O_3 and Ag/WSeS/β-Ga_2O_3.

The poor rectification of the pristine Ag/β-Ga_2O_3 contact originates from the strong Ag-derived interface states. Interlayer insertion offers a practical route to modify this interfacial coupling. Here, h-BN and Janus WSSe are introduced as two distinct interfacial modifiers: h-BN primarily acts as a weakly interacting spacer that suppresses the penetration of MIGS, whereas Janus WSSe introduces an intrinsic out-of-plane dipole that reshapes the local electrostatic potential and the tunneling barrier.

Fig. 5(a) and Fig. 6 show the I–V transport characteristics, PLDOS and spectral-current distributions of the Ag/h-BN/β-Ga_2O_3 contact. For the Ag/h-BN/β-Ga_2O_3 contact, the h-BN monolayer partially decouples the Ag electrode from the β-Ga_2O_3, substantially suppressing the MIGS extending into the semiconductor side. The suppression of the MIGS is directly visualized by the layer-resolved PDOS in Fig. S4 of the supplementary material, which compares the PDOS of the individual metal and β-Ga_2O_3 layers of the Ag/h-BN/β-Ga_2O_3 [Fig. S4(a)] and Ag/β-Ga_2O_3 [Fig. S4(b)] contacts: whereas the Ag-derived states in the bare contact remain appreciable several β-Ga_2O_3 layers away from the interface, they become essentially confined to the metal and interlayer region after h-BN insertion, leaving the deeper semiconductor layers free of gap states. The Fermi-level pinning is thus substantially alleviated, and a well-defined band gap is recovered in the semiconductor away from the immediate interface.

In the pristine Ag/β-Ga_2O_3 contact, MIGS-induced interfacial states enhance tunneling under both bias polarities, thereby weakening the rectifying behavior. After h-BN insertion, the suppression of these states reduces the contribution of interface-assisted tunneling, resulting in an I–V response that recovers forward rectification, as compared with Fig. 5(a), with the rectification ratio increasing from $\sim$0.22 to $\sim$6.35 (i.e., the rectification polarity is reversed) and the Schottky barrier height is 0.179 eV, as summarized in Table S3 of the supplementary material. Fig. 6(a), relative to (c), displays more strongly suppressed reverse-bias transport, whereas (b), in contrast to (d), shows carrier injection governed predominantly by transmission over the effective barrier under forward bias. These results establish that h-BN does not simply function as an additional insulating layer; rather, it improves the Ag contact by screening the electronic interaction responsible for MIGS and by

shifting the dominant transport contribution from tunneling toward thermionic emission, as shown in Fig. 6. To quantify this transition of the dominant transport mechanism, we extracted the ideality factor from the forward I–V characteristics, $n = (q/k_BT)\,\mathrm{d}V/\mathrm{d}(\ln|I|)$, over the forward-conducting bias window $V = -0.05$ to -0.3 V (Fig. S6 and Table S4). The values are $n \approx 11.3$ for Ag, 2.2 for Ag/h-BN, 5.5 for Ag/WSSe and 8.7 for Ag/WSeS. The pristine Ag contact exhibits $n \gg 1$, confirming tunneling- and interface-state-dominated transport, whereas after h-BN insertion n decreases to ≈ 2.2, a fivefold reduction indicating a substantial shift toward thermionic-emission-dominated transport; the Janus contacts again show $n \gg 1$, consistent with the tunneling-dominated transport revealed by the spectral-current analysis.

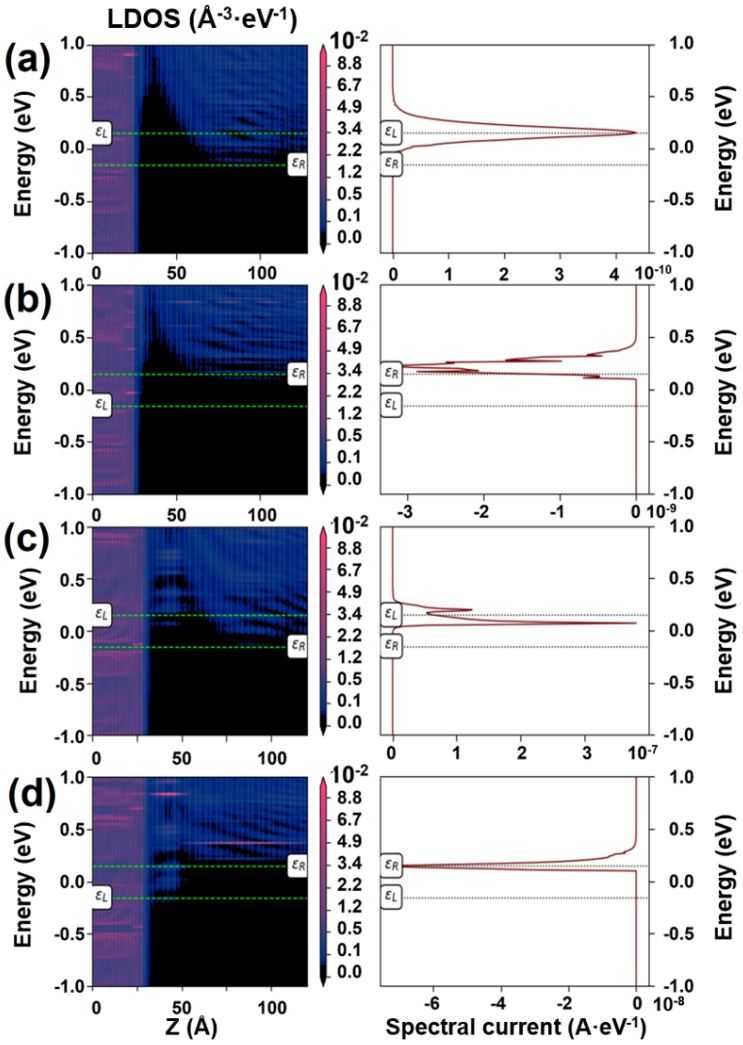


Figure 6: PLDOS and spectral current of Ag-based contacts with and without h-BN interlayer under different biases: (a–b) Ag/h-BN/β-Ga_2O_3 at (a) +0.3 V and (b) −0.3 V; (c–d) Ag/β-Ga_2O_3 at (c) +0.3 V and (d) −0.3 V.

A qualitatively different modulation is achieved by introducing a Janus WSSe interlayer. Unlike nonpolar h-BN, Janus WSSe induces an orientation-dependent electrostatic perturbation at the interface. In the WSSe configuration, the S-terminated side faces Ag and the Se-terminated side faces β-Ga_2O_3; the WSeS configuration corresponds to the reversed orientation. The transport response of the Janus-interlayered contacts is summarized in Fig. 5(b) and Fig. 7, which presents the I–V characteristics together with the PLDOS and

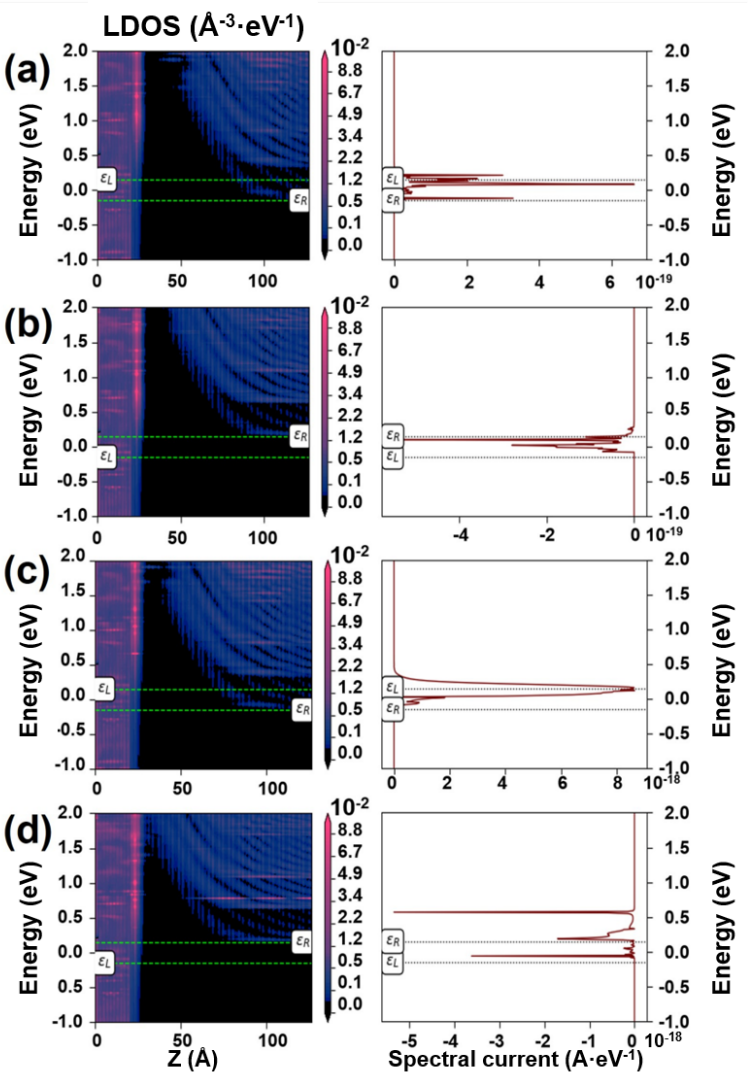


Figure 7: PLDOS and spectral current of Janus interlayers under different biases: (a–b) Ag/WSeS/β-Ga_2O_3 at (a) +0.3 V and (b) −0.3 V; (c–d) Ag/WSSe/β-Ga_2O_3 at (c) +0.3 V and (d) −0.3 V.

spectral-current distributions for Ag/WSeS/β-Ga_2O_3 and Ag/WSSe/β-Ga_2O_3. For the WSSe orientation, the built-in electric field interacts strongly with the depletion field on the β-Ga_2O_3 side, producing pronounced interfacial band bending. As shown in Fig. 5(b), the Ag/WSSe/β-Ga_2O_3 contact exhibits tunneling-dominated transport yielding reverse rectification. The PLDOS and spectral-current distributions in Fig. 7 further reveal that the polar interlayer introduces a field-induced modification which narrows the effective barrier and makes quantum tunneling the dominant transport channel, with only a negligible thermionic-emission contribution. The current response is consequently governed by the bias-dependent tunneling probability rather than by conventional thermionic injection, and this behavior leads to reverse rectification. These results demonstrate that a polar interlayer can deliberately reverse the transport asymmetry of the Ag/β-Ga_2O_3 contact.

When the Janus layer is reversed to the WSeS orientation, the intrinsic out-of-plane dipole is reversed; however, the total electrostatic-potential step across the interlayer increases in magnitude by 0.38 V rather than simply mirroring that of WSSe, and the resulting transport behavior is not a simple mirror image of that of WSSe. The altered interfacial coupling produces a weaker modification of the barrier profile and, consequently, a

smaller tunneling current, which is about 40 times smaller than that of the WSSe configuration. This distinction confirms that the transport response is controlled jointly by the electrostatic dipole and the chemical character of the terminating chalcogen layer, rather than by dipole reversal alone, as shown in Fig. 5(b).

Nevertheless, a direct comparison with the h-BN interlayer strategy highlights a critical limitation of the Janus configuration. Whereas h-BN insertion restores forward rectification with a sizable on-state current of $\sim$0.49 μA/μm at -0.3 V (Fig. 5), the Janus WSSe contact exhibits an extremely small absolute current magnitude under the operating bias, with a current of only $\sim 5.6\times10^{-9}$ μA/μm at $+0.3$ V—about 8.8×10^{7} times smaller (about eight orders of magnitude) than that of the h-BN interlayer. This severely limited current level—despite its novel polarity-reversal capability—constitutes a major disadvantage relative to the h-BN approach for practical ultra-wide-bandgap power-electronic applications. Therefore, alternative two-dimensional (2D) polar materials exhibiting intrinsically stronger tunneling-transport characteristics may be explored as interlayers to replace WSSe [33,34].

The distinct behavior of the two interlayers originates from their different electronic structure. The h-BN monolayer has a very large band gap (6.07 eV) and correspondingly large band offsets with respect to β-Ga_2O_3 (CBO $\approx$ 0.66 eV and VBO $\approx$ 0.65 eV), and it introduces only a small electrostatic-potential step ($\Delta V \approx -0.03$ V) across the layer, consistent with its nonpolar character; its states lie far outside the semiconductor gap, so that it blocks the evanescent metal wave functions without introducing new in-gap states. The Janus WSSe layer, in contrast, possesses an intrinsic out-of-plane dipole. We quantify the electrostatic-potential step across the interlayer as $\Delta V = V_{\mathrm{Janus/Ga_2O_3}} - V_{\mathrm{Ag/Janus}}$, evaluated in the vacuum regions on either side of the layer: the device values are $\Delta V = -1.76$ V for WSSe and -2.14 V for WSeS, i.e., reversing the layer increases the magnitude of the potential step by 0.38 V. This is much larger than the face-to-face potential difference of an isolated WSSe monolayer ($\approx$ 0.73–0.82 eV), because the device ΔV superposes the two contact-induced interface dipoles and the intrinsic Janus dipole with the electrode work-function difference, $\Delta V_{\mathrm{total}} = \Delta V_{\mathrm{Ag/Janus}} + \Delta V_{\mathrm{Janus,intrinsic}} + \Delta V_{\mathrm{Janus/Ga_2O_3}}$. This built-in field modifies the local band alignment and changes the effective barrier from 1.06 eV for the WSSe orientation to 1.69 eV for the reversed WSeS orientation. Because the Janus layer has a much smaller gap and its band edges lie close to the β-Ga_2O_3 gap, the field-induced barrier modification makes tunneling the dominant channel and leads to reverse rectification with a very small current. The pronounced dependence of the effective barrier on the layer orientation (1.06 versus 1.69 eV) shows that the transport response is controlled jointly by the electrostatic dipole and by the chemical character of the terminating chalcogen layer, rather than by dipole reversal alone. In practice this makes h-BN the more attractive of the two interlayers, since it restores forward rectification while retaining a sizable on-state current of 0.49 μA/μm, whereas the Janus contacts suffer from an extremely small current.

Finally, it is worth emphasizing the relationship between the Schottky barrier and rectification. Because the barrier height alone does not determine the transport asymmetry, the rectifying behavior is governed by the mechanism by which carriers cross the interface. The h-BN interlayer provides a clear illustration: inserting it changes the calculated barrier only from about 0.145 to 0.179 eV, yet the rectification ratio increases from about 0.22 to 6.35, i.e., the polarity reverses. This change is not caused by the small barrier modification but by the suppression of the Ag-derived MIGS. The MIGS decay length decreases from about 9.7 to 1.93 Å and the in-gap density of states at the Fermi level drops by more than an order of magnitude, which removes the

interface-assisted tunneling channels and shifts the dominant transport from tunneling to thermionic emission, as reflected in the decrease of the ideality factor from about 11.3 to 2.2. The polar Janus interlayers, in contrast, remain tunneling-dominated and reverse-rectifying. The metal-dependent trends follow the same logic: Au, with weak MIGS, preserves a well-defined barrier and forward, thermionic-dominated rectification, whereas Ag, Ti, and Ni have their barrier profiles reshaped by interface states and exhibit degraded or reversed rectification. The rectification polarity therefore tracks the interfacial electronic structure and the resulting transport mechanism rather than the absolute barrier height.

Overall, the h-BN and Janus-WSSe results demonstrate two complementary interlayer-engineering strategies for Ag/β-Ga_2O_3 contacts. h-BN suppresses Ag-induced gap states and restores forward rectification by reducing interface-assisted tunneling and favoring thermionic carrier injection. In contrast, Janus WSSe uses its intrinsic polarization to reshape the interfacial potential and promote tunneling-dominated reverse rectification. Thus, interlayers can be used not only to mitigate detrimental MIGS but also to deliberately tailor the barrier profile and rectifying polarity of β-Ga_2O_3-based Schottky contacts.

4. Conclusion

In this work, first-principles calculations combined with nonequilibrium Green's-function transport simulations were used to clarify the roles of donor concentration, metal species, and interlayer insertion in regulating Schottky transport at metal/β-Ga_2O_3(100) interfaces. For bare contacts, Au exhibits the most pronounced forward rectification among the metals considered at $1 \times 10^{19}\,\mathrm{cm}^{-3}$. In the Au/$\beta$-$Ga_2O_3$ contact, reducing the donor concentration leads to reverse rectification, whereas increasing it to $1 \times 10^{20}\,\mathrm{cm}^{-3}$ drives the contact toward quasi-ohmic transport. These trends arise from doping-induced changes in the barrier width and the resulting balance between thermionic emission and quantum tunneling. By comparison, strong MIGS in the Ag contact enhance Fermi-level pinning and interface-assisted tunneling, thereby weakening its rectifying behavior. Interlayer engineering provides effective control over this interface-limited transport. An h-BN monolayer weakens direct Ag/β-Ga_2O_3 coupling, suppresses Ag-induced gap states, and restores forward rectification by reducing tunneling leakage. In contrast, a Janus WSSe interlayer uses its intrinsic out-of-plane polarization to modify the local electrostatic potential and tunneling barrier, resulting in orientation-dependent and tunneling-dominated reverse rectification. These findings demonstrate that donor doping, metal selection, and interlayer design provide complementary routes for tailoring carrier injection and rectifying polarity in β-Ga_2O_3-based Schottky contacts.

See supplementary material for the calibration of the TB-mBJ parameter and of the HSE06 exchange-mixing parameter, the band structure of bulk β-Ga_2O_3, the interface models and lattice parameters, the calculated Schottky barrier heights and rectification ratios, the layer-resolved PDOS and the quantitative analysis of the MIGS penetration, the device-length convergence, the ideality factors, and the band offsets and interfacial potential steps of the interlayered contacts.

Acknowledgment

This work was supported in part by the National Key Research and Development Program of China (Grant No. 2024YFA1408200), the National Natural Science Foundation of China (Grant Nos. 12404099, 2534013, and 12504326), and the Science and Technology Innovation Program of Hunan Province (Grant Nos. 2025ZYJ001 and 2021RC4026).

Data Availability Statement

The data that support the findings of this study are available from the corresponding author upon reasonable request.

References

[1] Millan J and Godignon P et al 2014 *IEEE Trans. Power Electron.* **29** 2155–2163

[2] Pearton S J and Ren F et al 2018 *J. Appl. Phys.* **124** 220901

[3] Zhang J, Dong P, Dang K, Zhang Y, Yan Q, Xiang H, Su J, Liu Z, Si M, Gao J, Kong M, Zhou H and Hao Y 2022 *Nat. Commun.* **13** 3900

[4] Sun S, Wang X and Li Z et al 2025 *Adv. Electron. Mater.* **11** 2300844

[5] Kim J 2017 *J. Mater. Chem. C* **5** 1513–1522

[6] Zhang J, Shi J, Qi D C, Chen L and Zhang K H L 2020 *APL Mater.* **8** 020906

[7] Galazka Z, Irmscher K, Uecker R, Bertram R, Pietsch M, Kwasniewski A, Naumann M, Schulz T, Schewski R, Klimm D and Bickermann M 2014 *J. Cryst. Growth* **404** 184–191

[8] Higashiwaki M, Sasaki K, Kuramata A, Masui T and Yamakoshi S 2012 *Appl. Phys. Lett.* **100** 013504

[9] Li H C, Zhang E R, Duan S J, Wu S, Zhong L, Chen H R, Li Y, Kang D D, Chen B, Yu X X and Dai J Y 2025 *Appl. Phys. Lett.* **127** 132202

[10] Wong M H and Higashiwaki M 2020 *IEEE Trans. Electron Devices* **67** 3925–3937

[11] Kim H 2021 *SN Appl. Sci.* **4** 16

[12] Yang C, Liang H W, Zhang Z Z, Xia X C, Zhang H Q, Shen R S, Luo Y M and Du G T 2019 *Chin. Phys. B* **28** 048502

[13] Wang W F, Wang J F, Zhang Y M, Li T K, Xiong R and Xu K 2020 *Chin. Phys. B* **29** 047305

[14] Zhong X Q, Wang J, Wang B Z, Wang H Y, Guo Q and Sheng K 2018 *Chin. Phys. B* **27** 087102

[15] Yu W, Feng J and Gui Q et al 2025 *J. Appl. Phys.* **137** 115701

[16] Farzana E, Zhang Z, Paul P K, Arehart A R and Ringel S A 2017 *Appl. Phys. Lett.* **110** 202102

[17] Ahmadi E, Koksaldi O S, Kaun S W, Oshima Y, Mishra U K and Speck J S 2018 *Appl. Phys. Lett.* **112** 122102

[18] Sumesh C K, Patel K D, Pathak V M and Srivastav R 2011 *Chin. Phys. Lett.* **28** 087201

[19] Tersoff J 1984 *Phys. Rev. Lett.* **52** 465–468

[20] Mele E J and Joannopoulos J D 1978 *Phys. Rev. B* **17** 1528–1539

[21] Bardeen J 1947 *Phys. Rev.* **71** 717–727

[22] Skachkov D, Liu S L, Wang Y, Zhang X G and Cheng H P 2021 *Phys. Rev. B* **104** 045429

[23] Tung R T 2014 *Appl. Phys. Rev.* **1** 011304

[24] Liu X and Choi S et al 2022 *Adv. Mater.* **34** 2108425

[25] Mönch W 2012 *J. Appl. Phys.* **111** 073706

[26] Xiang Z, Luo J W and Li S S 2025 *Nat. Commun.* **16** 10675

[27] An X, Fan C H, Huang R and Zhang X 2009 *Chin. Phys. Lett.* **26** 087304

[28] Ramesh M and Niranjan M et al 2020 *AIP Conf. Proc.* **2220** 090017

[29] Karki Y, Aljeailan H, Irziqat M, Weerahennedige H, Wang H, Narayanan B, Sumanasekera G, Yu M and Jasinski J B 2025 *Nano Res.* **18** 94907547

[30] Xu R, Cheng L and Ma X et al 2025 *ACS Omega* **10** 9106–9112

[31] Li H, Li D, Tang P, Chen B, Pan C, Long G, Liu E, Jiang X, Zhang G, Qin S and Lu G 2015 *Nanoscale* **7** 15093–15098

[32] Zhang J, Wang J and Chen P et al 2017 *Nat. Nanotechnol.* **12** 744–749

[33] Liu Q, Zhu Z, Xie H Q, Fan Z Q, Wu D and Chen K Q 2025 *Appl. Phys. Lett.* **127** 092104

[34] Liu Q, Huang X D, Chen J J, Wu D, Deng X Q, Fan Z Q, Xie H Q and Chen K Q 2025 *Appl. Phys. Lett.* **126** 253502

[35] Li W F, Liu T W, Yang Z M, Wang L W and Liu Y Y 2025 *Chin. Phys. Lett.* **42** 017302

[36] Xu G H, Chen S Y and Liu Y Y 2026 *Chin. Phys. B* **35** 097201

[37] Xiang Z, Luo J W and Li S S 2026 *Phys. Rev. B* **113** 125304

[38] Liu Y Y, Lu H, Wang Z, Zeng L, Deng H X, Wei Z, Wang L W, Luo J W and Wang R 2025 *Phys. Rev. Appl.* **23** 034020

[39] Sun R, Xu H, He X, Xu X, Du S, Zhang K H and Long H 2025 *Surf. Interfaces* **72** 106949

[40] Liu Y Y, Xu G H, Xiong T, Li W F, Zhao Y, Liu T W, Wang Z, Wang R, Wang L W and Jiang X W 2024 *2024 IEEE International Electron Devices Meeting (IEDM)* pp 1–4

[41] Feng J, Yu W, Zhou E, Tang X, Liang J, Li X, Cheng S, Guo Y, Robertson J, Liu S and Zhang Z 2026 *Appl. Phys. Lett.* **128** 081604

[42] Feng J, Yu W, Liu T, Wang T, Gui Q, Zhou H, Guo Y, Liu S, Robertson J and Zhang Z 2026 *Nano Lett.* **26** 8775–8783

[43] Perdew J P, Burke K and Ernzerhof M 1996 *Phys. Rev. Lett.* **77** 3865–3868

[44] Tran F and Blaha P 2009 *Phys. Rev. Lett.* **102** 226401

[45] Becke A D and Johnson E R 2006 *J. Chem. Phys.* **124** 221101

[46] Koller D, Tran F and Blaha P 2012 *Phys. Rev. B* **85** 155109

[47] Lovejoy T C, Yitamben E N, Shamir N, Morales J, Villora E G, Shimamura K, Zheng S, Ohuchi F S and Olmstead M A 2009 *Appl. Phys. Lett.* **94** 081906

[48] Brandbyge M, Mozos J L, Ordejón P, Taylor J and Stokbro K 2002 *Phys. Rev. B* **65** 165401

[49] Taylor J, Guo H and Wang J 2001 *Phys. Rev. B* **63** 245407

[50] Stradi D and Martinez L et al 2016 *Phys. Rev. B* **93** 155302

[51] Smidstrup S, Stokbro K, Blom A, Markussen T, Wellendorff J, Schneider J, Gunst T, Verstichel B, Khomyakov P A, Vej-Hansen U G and Brandbyge M et al 2020 *J. Phys.: Condens. Matter* **32** 015901